Journal of Structural Biology 215 (2023) 108028

Contents lists available at ScienceDirect

Journal of Structural Biology

journal homepage: www.elsevier.com/locate/yjsbi

Research Article

Domain crossover in the reductase subunit of NADPH-dependent assimilatory sulfite reductase

Nidhi Walia [a,b], Daniel T. Murray [a,b,c], Yashika Garg [a,b], Huan He [b,d], Kevin L. Weiss [e], Gergely Nagy [e], M. Elizabeth Stroupe [a,b,*]

[a] Department of Biological Science, Florida State University, 91 Chieftain Way, Tallahassee, FL 32306, USA
[b] Institute of Molecular Biophysics, Florida State University, 91 Chieftain Way, Tallahassee, FL 32306, USA
[c] Molecular Biophysics and Integrated Bioimaging Division, Lawrence Berkeley National Laboratory, 1 Cyclotron Rd, Berkeley, CA 94720, USA[1]
[d] Translational Science Laboratory, College of Medicine, 1115 West Call Street, Tallahassee, FL 32306, USA
[e] Neutron Scattering Division, Oak Ridge National Laboratory, Oak Ridge, TN, USA

ARTICLE INFO

Keywords:
Sulfur metabolism
NADPH-dependent sulfite reductase
Diflavin reductase
Redox enzyme
Small-angle neutron scattering
Mass spectrometry

ABSTRACT

NADPH-dependent assimilatory sulfite reductase (SiR) from *Escherichia coli* performs a six-electron reduction of sulfite to the bioavailable sulfide. SiR is composed of a flavoprotein (SiRFP) reductase subunit and a hemoprotein (SiRHP) oxidase subunit. There is no known high-resolution structure of SiR or SiRFP, thus we do not yet fully understand how the subunits interact to perform their chemistry. Here, we used small-angle neutron scattering to understand the impact of conformationally restricting the highly mobile SiRFP octamer into an electron accepting (closed) or electron donating (open) conformation, showing that SiR remains active, flexible, and asymmetric even with these conformational restrictions. From these scattering data, we model the first solution structure of SiRFP. Further, computational modeling of the N-terminal 52 amino acids that are responsible for SiRFP oligomerization suggests an eight-helical bundle tethers together the SiRFP subunits to form the SiR core. Finally, mass spectrometry analysis of the closed SiRFP variant show that SiRFP is capable of inter-molecular domain crossover, in which the electron donating domain from one polypeptide is able to interact directly with the electron accepting domain of another polypeptide. This structural characterization suggests that SiR performs its high-volume electron transfer through both inter- and intramolecular pathways between SiRFP domains and, thus, *cis* or *trans* transfer from reductase to oxidase subunits. Such highly redundant potential for electron transfer makes this system a potential target for designing synthetic enzymes.

1. Introduction

Escherichia coli's dodecameric NADPH-dependent assimilatory sulfite reductase (SiR) is both asymmetric and highly flexible despite the potential for at least 4-fold symmetry (Murray et al., 2022). This extreme dynamism has challenged structural analysis of this essential oxidoreductase that reduces sulfite by six electrons to make sulfide, the bioavailable form of sulfur that is found in biological molecules like cysteine, methionine, biotin, and other sulfur-containing small molecule cofactors. SiR's efficient, high-volume electron transfer reactions, along with the absence of partially reduced intermediates produced by this homolog, generates a possibility for SiR to serve as a template for synthetic enzyme design efforts to aid in bioremediation of environmental sulfites (Lancaster, 2018; Mirts et al., 2018).

Abbreviations: SiR, sulfite reductase; SiRFP, sulfite reductase flavoprotein; NOS, nitric oxide synthase; SiRHP, sulfite reductase hemoprotein; CPR, cytochrome p450 reductase; Fld, flavodoxin-like FMN-binding domain; FNR, FAD-binding ferredoxin/NAD^+ reductase domain; SiRFP-60△, 60 kDa, monomeric, linker-truncated SiRFP; SiRFP-△, sulfite reductase flavoprotein linker truncation; SiRFP-X, sulfite reductase flavoprotein crosslinked; SANS, small-angle neutron scattering; NCV, neutron contrast variation; nLC-MS/MS, nano-liquid chromatography tandem mass spectrometry; 6xHis, polyhistidine tag; CBP, calmodulin-binding peptide tag; WT, wild-type; LB, Luria Bertani; SEC, size exclusion chromatography; DSiR, partially-deuterated SiR components with appropriate designation; his-SiRFP-X, 6xHis SiRFP-X_H132Q; CBP-SiRFP-X, CBP SiRFP-X_D545E; mSiRFP-X, mixed SiRFP-X; ABC, ammonium bicarbonate; FDR, False Discovery Rate; DT, sodium dithionite; CMP, contrast match point; SLD/ρ, scattering length density.

* Corresponding author at: Department of Biological Science, Florida State University, 91 Chieftain Way, Tallahassee, FL 32306, USA.
E-mail address: mestroupe@bio.fsu.edu (M. Elizabeth Stroupe).

[1] Current address.

https://doi.org/10.1016/j.jsb.2023.108028
Received 25 June 2023; Received in revised form 8 September 2023; Accepted 10 September 2023
Available online 12 September 2023

SiR is composed of two subunits that respectively accomplish the reductase and oxidase functions required for its activity. The reductase function of SiR is mediated by a flavoprotein subunit (SiRFP, α) that belongs to a class of diflavin reductases that includes the reductase domain of the chimeric oxidoreductase nitric oxide synthase (NOS) (Zhang et al., 2001) and reductases that transiently bind to various cytochromes (Wang et al., 1997). The oxidase subunit of SiR is a unique siroheme- and Fe_4S_4-dependent hemoprotein (SiRHP, β). What further sets SiR apart from other diflavin reductase-dependent enzymes is that SiRFP spontaneously forms an octamer when it is expressed in its full-length form (Siegel and Davis, 1974). The SiRFP octamer binds four SiRHP subunits independently at interfaces distal to SiRFP's octamerization domains (Murray et al., 2022; Siegel and Davis, 1974). In contrast, SiRHP is a monomer when isolated from the dodecameric holoenzyme or expressed independently (Crane et al., 1995; Siegel and Davis, 1974; Smith and Stroupe, 2012).

SiRFP belongs to a class of diflavin reductases that typically consist of four domains (Fig. 1A). The role of the N-terminal domain varies amongst these enzymes. In the case of cytochrome p450 reductase (CPR), it tethers the protein to the endoplasmic reticulum or mitochondrial membrane (Mitani, 1979). In the case of SiRFP, it organizes octamerization (Zeghouf et al., 2000). To date, there is no structure of this element of SiR. Moving towards the C-terminus from the octamerization domain, there is a region predicted to be unstructured followed by a flavodoxin-like, FMN-binding domain (Fld). Another unstructured linker that is longer than its homologous counterparts follows, leading to the connection domain that bridges the elements of an FAD-binding ferredoxin/NAD^+ reductase domain (FNR). These many unstructured regions are essential for the enzyme's activity but contribute to the challenge of obtaining a complete understanding of the dodecameric complex's structure (Askenasy et al., 2018; Gruez et al., 2000). Thus, the only atomic-resolution structures of the Fld and FNR domains of SiRFP are from an N-terminally truncated, monomeric form of 60 kDa (SiRFP-60△) that also has a six amino acid deletion within the internal linker bridging Fld and FNR domains (Tavolieri et al., 2019).

Within the SiR dodecameric holoenzyme, electrons move within SiRFP from a transiently bound NADPH to a stably-bound FAD, then to a stably-bound FMN, and finally to SiRHP, using three NADPH molecules for the complete cycle. The impact of SiR's oligomeric state on its function is unknown because we do not know the structure of the complex. Given the flexibility of this class of diflavin reductases, its two mobile domains could interact for electron transfer in at least two ways: the Fld and FNR domains from the same polypeptide could bind intramolecularly or those domains from different polypeptides could bind intermolecularly by domain crossover (Fig. 1B) (Rousseau et al., 2003; Schaefer et al., 2011). Thus, these variable structural interactions suggest the possibility that the FNR domain of one polypeptide could transfer electrons to the Fld domain of another polypeptide. Further, the Fld domain could then interact in *cis* with a SiRHP bound to the same SiRFP or in *trans* with a SiRHP bound to an adjoining SiRFP (Fig. 1C). In the context of the known complex interactions between the subunits (Askenasy et al., 2018; Murray et al., 2021; Murray et al., 2022), we hypothesize that the numerous binding partner permutations suggest electrons could move through any of these redundant interaction networks within the SiR dodecamer.

To better understand the conformationally malleable SiRFP octamer, we generated conformationally-restricted variants of SiRFP that either lock its flavin-binding domains in an open conformation by shortening the linker between the domains (SiRFP-△), as in the monomeric form we previously crystallized (Tavolieri et al., 2019), or crosslinked in a closed conformation via an engineered disulfide bond (SiRFP-X). Biochemical, small-angle neutron scattering (SANS), neutron contrast variation (NCV), and nano-liquid chromatography tandem mass spectrometry (nLC-MS/MS) analyses show that even with conformational restriction in SiRFP, the complex remains asymmetric and flexible. Further, engineered cysteine crosslinks within the SiRFP subunit reveal

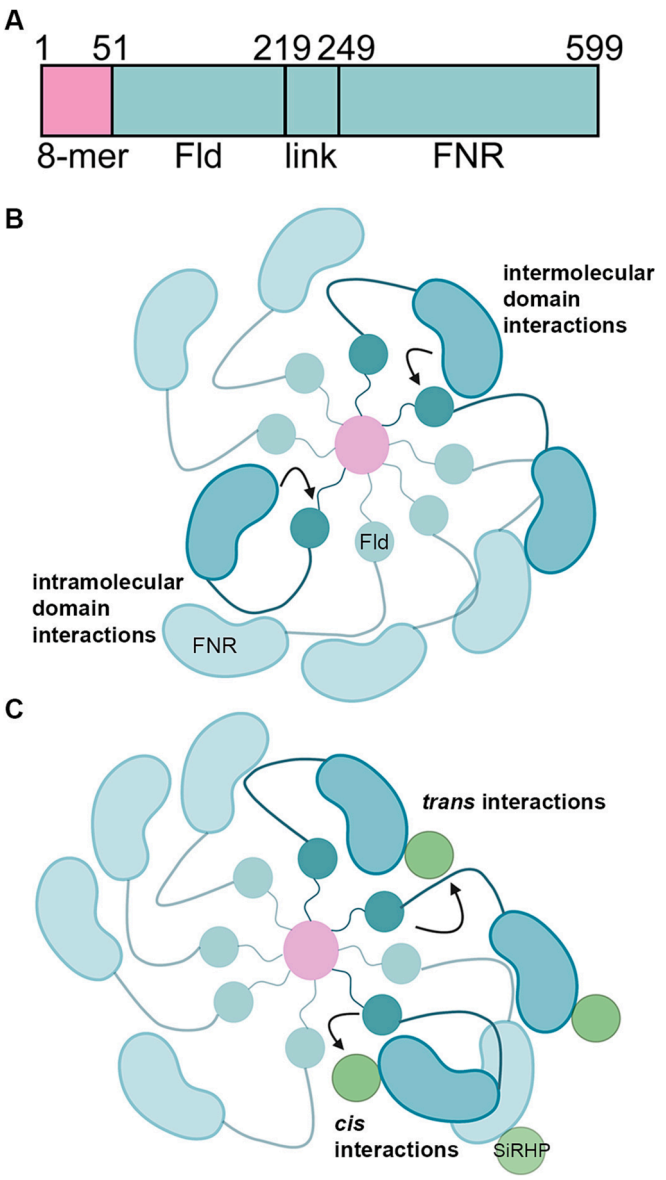

Fig. 1. SiR is a modular oxidoreductase with extensive potential for domain crossover. (A) A schematic of SiRFP's domain composition. The N-terminal octamerization (8-mer) domain is pink and the Fld, 30-residue linker (link), and FNR domains are teal. (B) Possible intramolecular interactions within a single polypeptide or intermolecular interactions through domain crossed subunits, in either case between an Fld and FNR domain. (C) Possible *cis* or *trans* interactions between SiRFP's Fld domain and a tightly-bound SiRHP or one bound to another SiRFP subunit, respectively.

interactions across subunits, akin to the *trans* domain crossover visualized in full-length NOS, where the reductase domain of one polypeptide interacts with the oxidase of another (Campbell et al., 2014; Haque et al., 2018; Siddhanta et al., 1998). By comparing oxidized and reduced SiRFP variants with SANS, we additionally show that the uniquely long linker between SiRFP's flavin binding domains contributes to the redox state-dependent conformational malleability within this essential enzyme.

2. Materials and methods

2.1. Generation of conformationally restricted variants

We designed two conformationally restricted variants in either full length SiRFP octamer (*cysJ*-pBAD (Askenasy et al., 2015)) or in the SiR

holoenzyme (*cysJIG*-pBAD (Askenasy et al., 2015)). In the first variant, two background cysteines (C162T and C552S) were altered to prevent unwanted crosslinking. Then, two cysteines were engineered at positions 121 and 556, forming a disulfide bond between Fld and FNR domains of SiRFP. Crosslinks were confirmed via MS, described below. We represent this construct (SiRFP_C162T_C552S_E121C_N556C) as SiRFP-X and in the SiR holoenzyme as SiR-X. The positions of these cysteines were chosen on the basis of crystal contacts identified in the crystal structure of monomeric SiRFP-60△ (Tavolieri et al., 2019). Q5 site directed mutagenesis (New England Biolabs, Ipswich, MA) was used to construct the mutations and DNA sequencing confirmed the presence of all desired mutations. The second set of conformationally restricted variants, SiRFP-△ and SiR-△, were generated by truncating six amino acids (positions 212–217, △-AAPSQS) from the linker joining the Fld and FNR domains in SiRFP as previously described (Tavolieri et al., 2019).

To assess whether the disulfide crosslinking in SiRFP-X formed inter- or intramolecularly (or a combination of both within the octamer), we generated two additional uniquely-tagged SiRFP-X expression constructs with further amino acid variation within the crosslinked polypeptides so peptides from different subunits could be identified via MS. The first pBAD expression construct contained an N-terminal polyhistidine tag (6xHis) with an additional alteration at position 132 (H132Q). The second pET28b expression construct contained an N-terminal calmodulin-binding peptide tag (CBP) with an additional alteration at position 545 (D545E).

2.2. Complementation assays

Complementation assays on conformationally restricted variants were performed as previously described (Askenasy et al., 2015). SiRFP-deficient *E. coli* (*cysJ*$^{-}$) cells (Baba et al., 2006) were separately transformed with plasmids expressing wild-type SiRFP (SiRFP-WT), empty pBAD vector, SiRFP-X, or SiRFP-Δ. Cells were grown overnight in Luria Bertani (LB) medium with 100 μg/ml ampicillin and 50 μg/ml kanamycin selection. All cells were centrifuged at 4000 × g for 10 mins and cell pellets were washed twice with M9 salts. Cell densities were normalized at OD_{600} before plating serial dilutions onto either M9 agar or LB medium plates with ampicillin and kanamycin selection.

2.3. Protein expression and purification

All SiRFP/SiR variants were expressed and purified as previously described (Askenasy et al., 2018; Askenasy et al., 2015; Murray et al., 2022). In brief, *E. coli* LMG194 cells (Invitrogen, Carlsbad, CA, USA) were transformed with a pBAD plasmid (Thermo Fisher Scientific, Waltham, MA, USA) containing genes encoding SiRFP-X, SiR-X, SiRFP-Δ or SiR-Δ. SiRFP-X/SiR-X expressing cells were grown overnight and SiRFP-Δ/SiR-Δ expressing cells were grown for 4 h in LB broth in the presence of ampicillin. Cultures were induced with 0.05% L-arabinose at 25 ℃. Protein purification of each hydrogenated protein was performed using Ni-NTA affinity chromatography (Cytiva, Marlborough, MA, USA), anion exchange HiTrap-Q HP chromatography (Cytiva, Marlborough, MA, USA) and size exclusion chromatography (SEC). SEC was performed using a Sephacryl S300-HR column (Cytiva, Marlborough, MA, USA) with previously optimized running buffers (Askenasy et al., 2018; Askenasy et al., 2015; Murray et al., 2022).

Partially-deuterated SiRHP (all partially deuterated SiR components or variants are abbreviated as DSiR with the appropriate designation) was purified as previously described. In brief, *E. coli* BL21 (DE3) cells (New England Biolabs, Ipswich, MA, USA) were transformed with a pBAD vector containing bicistronic *cysI* and *cysG* (siroheme synthase). DSiRHP was expressed in Enfors minimal media containing 70% D_2O, at 25℃ with 0.05% L-arabinose and purified using a combination of ammonium sulfate precipitation, desalting, anion exchange and gel filtration chromatography (Murray et al., 2021; Murray et al., 2022).

Reconstituted, partially-deuterated DSiR-X complex was assembled as previously described for DSiR (Murray et al., 2022). In brief, purified SiRFP-X was mixed with 6 M equivalents DSiRHP followed by 2 h incubation on ice. Next, the reconstituted complex was applied to Ni-NTA affinity column and then loaded onto a HiPrep 26/60 Sephacryl S-300 HR column. This two-step purification of reconstituted DSiR-X removes excess DSiRHP and results in a single species as confirmed by UV–vis spectroscopy, SEC, and SDS-PAGE analysis.

For expressing mixed crosslinked variants, BL21 (DE3) *E. coli* cells were co-transformed with pBAD plasmid encoding 6xHis SiRFP-X_H132Q (his-SiRFP-X) and pET28b plasmid encoding CBP SiRFP-X_D545E (CBP-SiRFP-X). We represent this variant as mixed SiRFP-X (mSiRFP-X). These co-transformed cells were induced in the presence of ampicillin and kanamycin, and then expressed overnight with 0.05% L-arabinose and 0.5 mM IPTG at 25 ℃. Protein purification was performed using Ni-NTA affinity and HiPrep 26/60 Sephacryl S-300 HR columns with 50 mM HEPES, pH 8.0, 150 mM NaCl as SEC running buffer. Western blot analysis with α-his (Rockland Immunochemical, Pottstown PA, USA) or α-CBP (Genscript, Piscataway, NJ, USA) antibodies confirmed the presence of both variants.

2.4. In-gel protein trypsin digestion

A wash buffer (50% acetonitrile in H_2O with 100 mM ammonium bicarbonate (ABC)) was used to de-stain carefully cut gel bands, which afterwards were further cut into ~ 1 mm pieces. Gel pieces were then dried and rehydrated with a digestion buffer (10% acetonitrile in H_2O with 50 mM ABC). MS grade trypsin (Thermo Fisher Scientific, Waltham, MA, USA) was added and the mixture was incubated at 37 ℃ for 2 h. A solution of 0.5% formic acid was added to quench the digestion. After the supernatant was collected, the remnant gel pieces were dried by incubation with acetonitrile and the supernatant was again collected. Combined supernatant was dried in a SpeedVac (Thermo Fisher Scientific, Waltham, MA, USA).

2.5. Nano-liquid chromatography tandem mass spectrometry

The tryptic peptide mixture was re-constituted in 5% acetonitrile in H_2O with 0.1% formic acid and loaded to an Easy nLC-1200I system (Thermo Fisher Scientific, Waltham, MA, USA) for separation. Peptides were initially concentrated and desalted with a nanoViper Acclaim PepMap 100 C18 100 μm × 2 cm trap column (Thermo Fisher Scientific, Waltham, MA, USA). The desalted peptides were then separated with a nanoViper Acclaim PepMap RSLC C18 75 μm × 15 cm analytical column (Thermo Fisher Scientific, Waltham, MA, USA). Mobile phases composition are as follows: A (99.9% H_2O with 0.1% formic acid) and B (90% acetonitrile with 0.1% formic acid). A stepwise linear gradient profile was as follows: from 0% to 1% B over 2 min, from 1% to 55% B over 60 min, from 55% to 95% B over 5 min, hold at 95% B for 15 min, from 95% to 1% B over 5 min and hold at 1% B for 10 min with a flow rate of 300 nL/min. The nLC was on-line with a high mass accuracy, high resolving power Orbitrap Exploris 480 Mass Spectrometer MS (Thermo Fisher Scientific, Waltham, MA, USA). nLC eluate was ionized with a nanospray ion source at 2.3 kV and detected. Precursor ions were detected in the Ultra-High-Field Orbitrap Mass Analyzer in the positive ion mode with a mass resolution of 120 K (at m/z of 200 Da) and a mass range of 300–1500 Da. The top 15 most abundant precursor ions were subjected to higher-energy collisional dissociation and the generated fragment ions were detected with a mass resolution of 15 K (at m/z of 200 Da) with a dynamic exclusion duration of 30 s and 10 ppm mass tolerance.

2.6. Mass spectrometry data analysis

MS data was acquired with the Xcalibur software (Thermo Fisher Scientific, Waltham, MA) and then analyzed with the Proteome Discoverer 2.5 software with Sequest HT (Thermo Fisher Scientific,

Waltham, MA) and XLinkX node (Liu et al., 2015) against the SiRFP protein sequence to identify both disulfide bond cross-linked peptides and non-cross-linked peptides. Dynamic modifications of methionine oxidation (+15.995 Da), N-terminal methionine-loss, and/or N-terminal acetylation were considered. Validation parameters were set with a 1% strict target False Discovery Rate (FDR) and a 5% relaxed target FDR. Disulfide bond cross-linked peptides were analyzed with a minimum S/N of 1.5, precursor mass error up to 10 ppm, and fragment ions mass error up to 30 ppm. Identified cross-linked peptides were then manually checked for confirmation of assignment.

2.7. Anaerobic protein reductions

Sodium dithionite (DT) was used to reduce the SiRFP, SiRFP-X and SiRFP-Δ in an anaerobic glove box containing a N_2 atmosphere, as previously described (Murray et al., 2021; Tavolieri et al., 2019). First, solutions containing 50 mM KPi, pH 7.8, 100 mM NaCl, 1 mM EDTA and 100% D_2O were degassed using freeze-pump/thaw cycling and inert gas substitution followed by dialysis of protein samples in the degassed buffer for ~ 6 h under anerobic conditions. 10 M equivalents of DT were added to each sample followed by 15 min incubation. The glove box was continuously purged with N_2 gas throughout to maintain an inert atmosphere.

2.8. SANS data collection

We used the previously determined contrast match point (CMP) of DSiR's components (CMP of DSiRHP is 86% D_2O and the CMP of hydrogenated SiRFP is 41% D_2O) (Dunne et al., 2017; Murray et al., 2021; Murray et al., 2022) for NCV measurements of DSiR-X. DSiR-X was dialyzed into buffer with varying H_2O:D_2O ratios (0%, 41%, 86%, or 100% D_2O) to obtain SANS measurements at the CMPs of DSiR-X's components, a full contrast measurement of the whole complex, as well as at contrast points flanking either CMP for a thorough NCV series. Hydrogenated SiRFPX, SiRFP-Δ, SiR-X and SiR-Δ proteins were dialyzed into buffer with 100% D_2O to obtain full contrast measurements with minimal incoherent scattering from hydrogen and maximized signal-to-noise ratios. Post-dialysis concentrations of all samples were measured using a Nanodrop One UV–vis spectrophotometer (Thermo Fisher Scientific, MA).

SANS data was collected on the Extended Q-Range Small-angle Neutron Scattering diffractometer (EQ-SANS, Beam Line-6) at the Spallation Neutron Source (SNS) at Oak Ridge National Laboratory (ORNL). Instrument configurations for SiRFP/SiR variants and the DSiR-X NCV series were the same as previous experimentation (Murray et al., 2022). In brief, three configurations were used in 60-Hz operation mode to encompass a q range covering SiR's length scales: 9 m sample-to-detector distance with 15 Å wavelength band, 4 m sample-to-detector distance with 6 Å wavelength band, and 1.3 m sample-to-detector distance with 4 Å wavelength band. The relevant wavevector transfer is represented by q, where $q = 4\pi\sin(\theta)/\lambda$, where 2θ is the scattering angle and λ is the neutron wavelength. For the reduced samples (SiRFP, SiRFP-X and SiRFP-△), a two-configuration setting was used: 4 m sample-to-detector distance with 10 Å wavelength band and 2.5 m sample-to-detector distance with 2.5 Å wavelength band, which covered a sufficient q range (0.005–0.7 $Å^{-1}$). Oxidized SiRFP variants (SiRFP, SiRFP-X and SiRFP-△) were measured again using the same configuration settings as for the reduced samples. All samples were loaded into 1 mm pathlength circular quartz cuvettes (Hellma USA, Plainville, NY, USA) and data was collected at 8 °C. Cuvettes containing reduced samples were sealed with rubber septa and parafilm. Dry air was simultaneously introduced during oxidized sample measurements to prevent condensation on the cuvette and N_2 gas was introduced during reduced sample measurements to maintain the anaerobic environment.

SANS data were circularly averaged and reduced to one-dimensional scattering profiles according to standard procedures using the *drtsans* software (Heller et al., 2022). Data were corrected for detector sensitivity, subtracted of scattering contributions from the buffer and empty cell, and then placed on an absolute scale using a calibrated porous silica standard. All replicate measurements were summed, followed by merging of data from different q ranges collected at each instrument configuration. Initial scattering profiles were compared with their duplicate measurements at the end of each data collection, showing no change and confirming sample integrity.

2.9. SANS data analysis and modelling

Guinier and dimensionless Kratky analyses were carried out in BioXTAS RAW (Hopkins et al., 2017; Murray et al., 2022). GNOM, from the ATSAS suite (Manalastas-Cantos et al., 2021), was used to calculate pairwise distance distribution ($P(r)$) functions, which subsequently provided real-space $I(0)$, R_g, and D_{max} values. D_{max} values were assessed based on both the shape of the $P(r)$ curve as it smoothly tapered off and the quality-of-fit assessment showing the overall fit estimate (X^2) of the theoretical scattering curve to the data. SANS MWs were also calculated using ATSAS. Stuhrmann and parallel axis theorem analyses (Moore, 1981; Moore et al., 1974; Olah et al., 1994) were performed using MULCh (Whitten et al., 2008) as previously described (Murray et al., 2022). In brief, the contrast derived from each scattering component of a mixed complex can be calculated by subtracting the scattering length density (SLD or ρ) of the solvent from the macromolecule ($\triangle\rho = \rho_{macromolecule} - \rho_{solvent}$). The Stuhrmann plot was generated to show the relationship between R_g and contrast based on parameters obtained using the following equation:

$$R_g^2 = R_m^2 + \alpha/\Delta\overline{\rho} - \beta/\Delta\overline{\rho}$$

where R_m is the R_g of the complex with homogenous distribution of scattering density, $\triangle\overline{\rho}$ is the mean contrast, and α and β are coefficients derived from the SLD (Ibel and Stuhrmann, 1975; Whitten et al., 2007). The α coefficient is the second moment of scattering density fluctuations and the β coefficient is the square of the first moment of density fluctuations. In a two-component system, *i.e.*, macromolecular complexes with two molecules possessing different SLD, the sign of α is related to the position of each component relative to their collective center of mass (COM) and β relates to the separation between each component's respective COM. The contrast and R_g analysis modules were used in MULCh to calculate $\triangle\overline{\rho}$, SLD, and the contrast dependence of R_g.

Ab initio SANS models were generated in DENSS (Grant, 2018) using GNOM $P(r)$.out files as input. The "enforce connectivity" parameter was set to "1" and 20 reconstructions were generated in "slow" mode, after which they were averaged, aligned, and refined without symmetry constraints. However, in the case of DSiR-X41 DENSS modelling, the "enforce connectivity" parameter was set to "4" and a single reconstruction was chosen to counter this measurement's lower signal-to-noise resulting from discrete, mobile, ~64 kDa DSiRHP subunits scattering amidst a substantial incoherent background at 41% D_2O in the context of a contrast-matched, hydrogenated SiRFP eight times its molecular weight. To validate the single best reconstruction of DSiR-X41, theoretical scattering was calculated from the DENSS model using the EM2DAM module in ATSAS (Manalastas-Cantos et al., 2021) and compared to the experimental data.

The structure of a single subunit of full length SiRFP including its N-terminus region was obtained using AlphaFold (Jumper et al., 2021; Roney and Ovchinnikov, 2022). The HDOCK (Yan et al., 2020) server was further used to model a putative octameric oligomer of the N-terminus. Eight copies of SiRFP lacking their N-terminal 52 amino acids along with the predicted octameric N-terminus oligomer were then independently placed into SiRFP-X's DENSS envelope. DSiR-X41's DENSS model were also superimposed with four SiRHP atomic models based on PDB 1AOP (Crane et al., 1995). All superimpositions of high resolution atomic models on solution scattering envelopes were done in

USCF ChimeraX (Pettersen et al., 2020). The positioning of the superimposed models was validated in two ways. First, theoretical scattering of the models was calculated with Fast X-Ray scattering (FOXS) (Schneidman-Duhovny et al., 2013), which uses the Debye formula to estimate scattering profiles from the superimposed high-resolution structures. Second, we repeated this analysis with the Polynomial Expansions of Protein Structures and Interactions (PEPSI-SANS) method (Grudinin et al., 2021), which uses a multipole-based scheme to estimate theoretical scattering.

3. Results

3.1. SiRFP undergoes domain crossover

The crystal structure of a monomeric form of SiRFP lacking its N-terminal octamerization domain shows the possibility for the Fld domain of one polypeptide to bind in a closed conformation with the FNR domain of a different polypeptide (Tavolieri et al., 2019). Whether this happens in the octameric SiRFP is unknown. Thus, considering the flexible nature of SiRFP-WT and the asymmetry observed in the SiR dodecamer (Murray et al., 2022), we hypothesized that the diflavin reductase domains are capable of domain crossover between opposing Fld and FNR domains within octameric SiRFP, perhaps to enable the large volume electron transfer needed to fully reduce SO_3^{2-} by six electrons in SiR's characteristically efficient fashion.

To test this hypothesis, we engineered a cysteine disulfide bond in a cysteine-free variant of SiRFP to crosslink the Fld and FNR domains between amino acids 121 (E121C) and 556 (N556C) (SiRFP-X; all variants are summarized in Supplemental Table S1). SiRFP-X remains active, albeit with slightly reduced ability to complement a SiRFP-deficient strain of *E. coli* (Fig. 2A). If our hypothesis is accurate, we predicted that we would see higher-order species of SiRFP-X in denaturing, but non-reducing, SDS-PAGE analysis. Indeed, in SiRFP-X, species at 67 kDa (monomer), 135 kDa (dimer), and upward to 270 kDa (tetramer) are observed (Fig. 2B). The purified protein retains the proper spectroscopic signals from its flavins and possesses a singular absorbance peak in its SEC profile, indicating it is properly folded (Fig. 2C and S1A). To confirm that the engineered crosslinks formed as anticipated (Fig. 2D and E), we performed proteolytic MS analysis on the 67 kDa and higher-order gel bands. We identified both non-crosslinked peptides corresponding to amino acids E121C and N556C as well as the corresponding crosslinked peptides containing those amino acids (Fig. 2B and F and S2A). Intramolecular crosslinks run as the non-crosslinked protein within the 67 kDa band.

We next aimed to show specifically that crosslinking was occurring through domain-crossed subunits. Therefore, we engineered an expression system that could generate populations of mixed SiRFP octamers for purification and subsequent analysis. We co-expressed 6xHis and CBP SiRFP-X subunits on either a pBAD or pET28b plasmid in the crosslink-forming variant. In the 6xHis construct, we introduced a variant at histidine 132 (H132Q) so the peptide containing E121C was uniquely identifiable but left the peptide around N556C as WT (his-SiRFP-X, Fig. 2E). In the CBP construct, we retained H132 as WT but engineered a further variant in the peptide around N556C so it was uniquely identifiable, D545E, (CBP-SiRFP-X, Fig. 2E). Western blot analysis of the purified complex showed that we isolated a mixed population of octamers, mSiRFP-X (Fig. S2B).

We repeated the denaturing, but non-reducing, SDS-PAGE analysis followed by proteolytic MS analysis on the 67 kDa and higher order bands from mSiRFP-X. MS showed all three possible combinations of crosslinking between his-SiRFP-X and CBP-SiRFPX. We observed crosslinked peptides amongst his-SiRFP-X subunits, CBP-SiRFP-X subunits and in between his-SiRFP-X and CBP-SiRFP-X subunits, providing the first direct evidence that SiRFP undergoes domain crossover (Fig. 2G-I (species 2–4) and S2C-E).

3.2. Conformationally-restricted SiRFP variants differ in their distance distribution and flexibility

The absence of symmetry in native SiR, demonstrated by prior SANS studies (Murray et al., 2022), suggests that the eight SiRFP subunits do not adopt the same open or closed conformations, not excluding a continuum of relative positions between the two extremes. The resulting exceptional potential for heterogeneity complicates high-resolution structural analysis, as demonstrated in monomeric SiRFP-60 that lacks the octamerization domain but contains a full-length linker (Gruez et al., 2000). Thus, we restricted SiRFP's ability to transition between the opened or closed conformations by shortening the linker between the Fld and FNR domains (SiRFP-△), a deletion previously used in SiRFP-60△ that allow us to crystallize both domains in a single structure (Tavolieri et al., 2019), and compared the neutron scattering from SiRFP-X and SiRFP-△.

Scattering from SiRFP-X compared to that from SiRFP-△ shows that, as expected, SiRFP-X is more compact than SiRFP-△ (Table 1, Fig. 3A and Table S2). SiRFP-X has an R_g of 78.5 ± 0.2 Å and D_{max} of 230 Å. SiRFP-△ has an R_g of 78.6 ± 0.7 Å and D_{max} of 255 Å. Guinier analysis of each dataset indicates monodisperse protein solutions, consistent with its SEC profile (Fig. S1A and S3A and B). Therefore, by crosslinking the Fld and FNR domains, the R_g does not change but the D_{max} is reduced from 255 Å to 230 Å. Previous analysis of SiRFP-WT showed an R_g of 80.8 ± 0.8 Å and D_{max} of 260 Å (Murray et al., 2022). This suggests that the crosslinked variant positioned its domains in a closed conformation, whereas SiRFP-△ is in a more open conformation, without affecting the distribution of mass as dramatically.

We used *P(r)* calculations to determine the probability of interatomic distance distributions for each variant and compared them to the previously determined WT analysis (Murray et al., 2022). The *P(r)* functions for each variant have an interatomic vector length *(r)* peak around 100 Å (Fig. 3B and S4A and B), slightly lower than the published value for the SiRFP-WT (110 Å) (Murray et al., 2022). However, they retain the shoulder at lower values of *r* that indicate distinct intra-subunit distances of differing scales within the complex.

Kratky analysis of small-angle scattering data provides a qualitative measure of flexibility, disorder, and folding for a proteinaceous scattering particle (Rambo and Tainer, 2011). The scattering data from SiRFP-X and SiRFP-△, upon transformation into dimensionless Kratky plots normalized by *I(0)* (mass and concentration) and non-dimensionalized (skewing the *q* by R_g), demonstrates that both variants are flexible as indicated by their plots each possessing plateaus at high qR_g (Fig. 3C). The single peak in the Kratky plot of SiRFP-△ shows a slightly higher and shifted maxima (1.7 for qR_g 2.59) compared to the standard (1.1 for qR_g $\sqrt{3}$) (Durand et al., 2010) indicating a well folded but asymmetric complex. However, in case of SiRFP-X, the Kratky plot shows a double peak feature, where the first peak shows the maxima closer to standard value (1.1 for qR_g 1.8) and other at (1.2 for qR_g 7.3). These two peaks may represent the mixed population of intra- and intermolecular crosslinked SiRFP-X. However, comparing higher *q* values ($qRg > 8$), SiRFP-X shows a more compact conformation whereas SiRFP-△ shows a more extended conformation, as expected.

3.3. SiRHP remains peripheral and asymmetrically organized when SiRFP is conformationally restricted

In WT SiR, SiRHP binds at the periphery of the SiRFP and results in an asymmetric organization of the complex, but it is not clear whether each SiRHP is bound to adjacent SiRFP monomers or whether they are distributed around the octamer (Murray et al., 2022). To assess whether the conformation of SiRFP impacts the positioning of SiRHP, we measured an NCV series scattering on SiR-X assembled from partially deuterated SiRHP (DSiRHP) and hydrogenated SiRFP-X (to make DSiR-X) in 0%, 41%, 86%, and 100% D_2O buffers (Fig. 4A). Reconstituted DSiR-X assembles in the correct stoichiometry, as judged by UV–vis

spectroscopy (Fig. 2C). Further, both SEC at 0% D_2O and Guinier analysis at each CMP show that it is monodisperse (Fig. S1B and S3C-F).

P(r) analysis shows that the scattering of the DSiRHP-matched complex (86% D_2O, DSiR-X86) has an overall R_g of 78.5 ± 0.4 Å and D_{max} of 226 Å (Table 1, Fig. 4B and Table S2). In contrast, there are five populations of interatomic distance peaks for the SiRFP-matched complex (41% D_2O, DSiR-X41) that arise from the bound SiRHP subunits ranging from 30 Å to a D_{max} of 324 Å, which is slightly larger than the D_{max} for the whole complex (Table 1, Fig. 4B, and Table S2,). The fits of the *P(r)* plots agree with the experimental data (Fig. S4C-F).

Stuhrmann analysis (Ibel and Stuhrmann, 1975; Whitten et al., 2007) shows that, unlike DSiR-WT (Murray et al., 2022), DSiR-X shows a near-

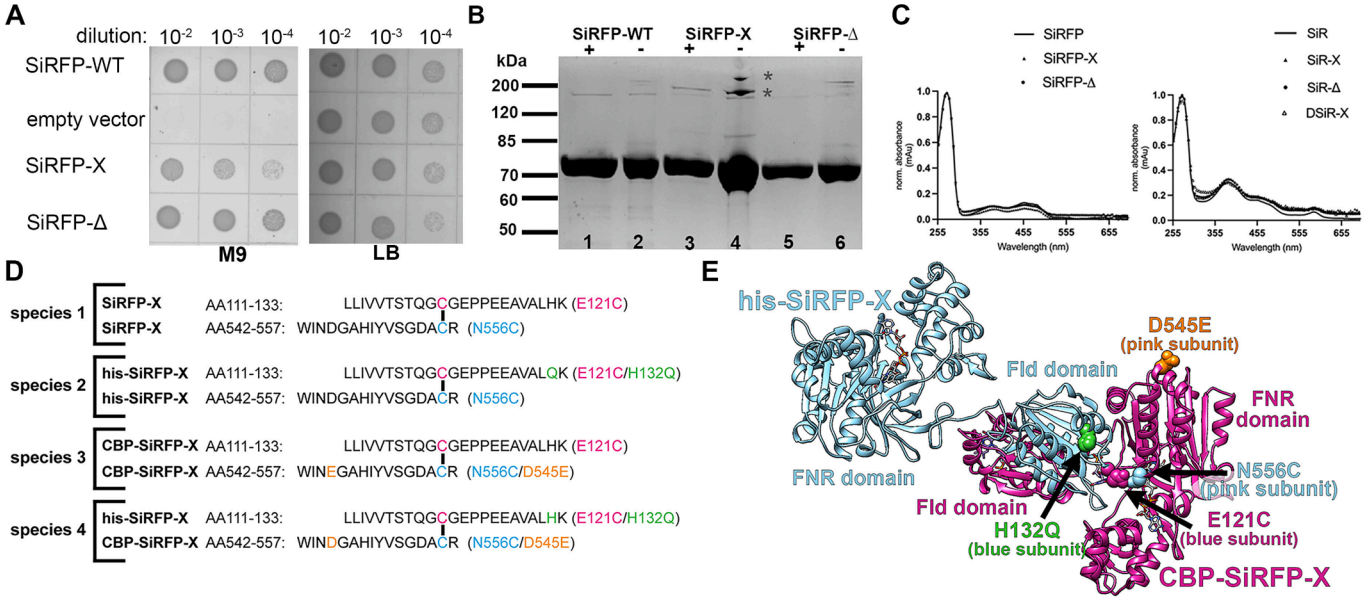

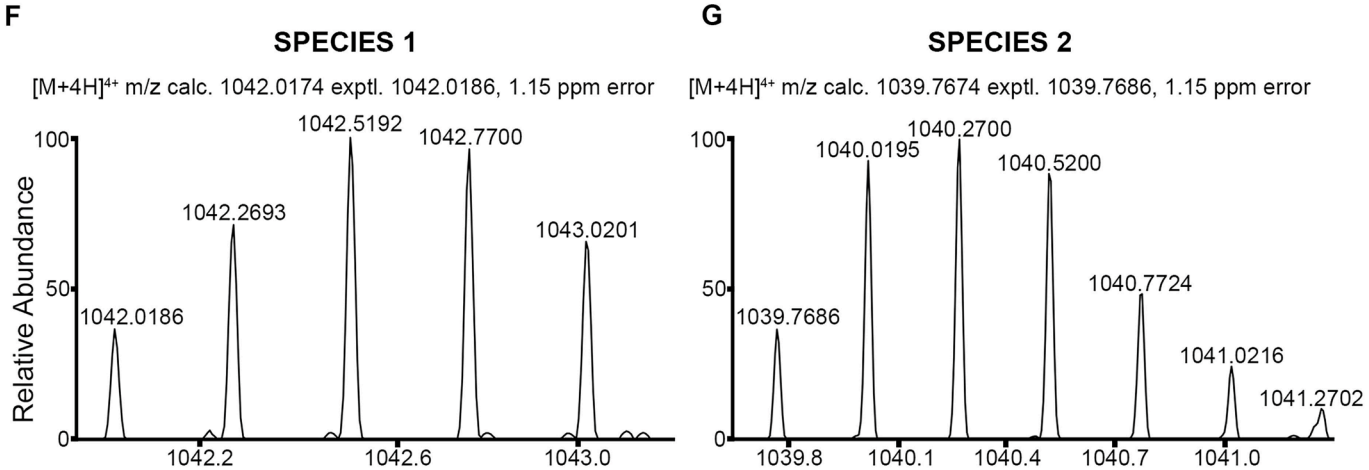

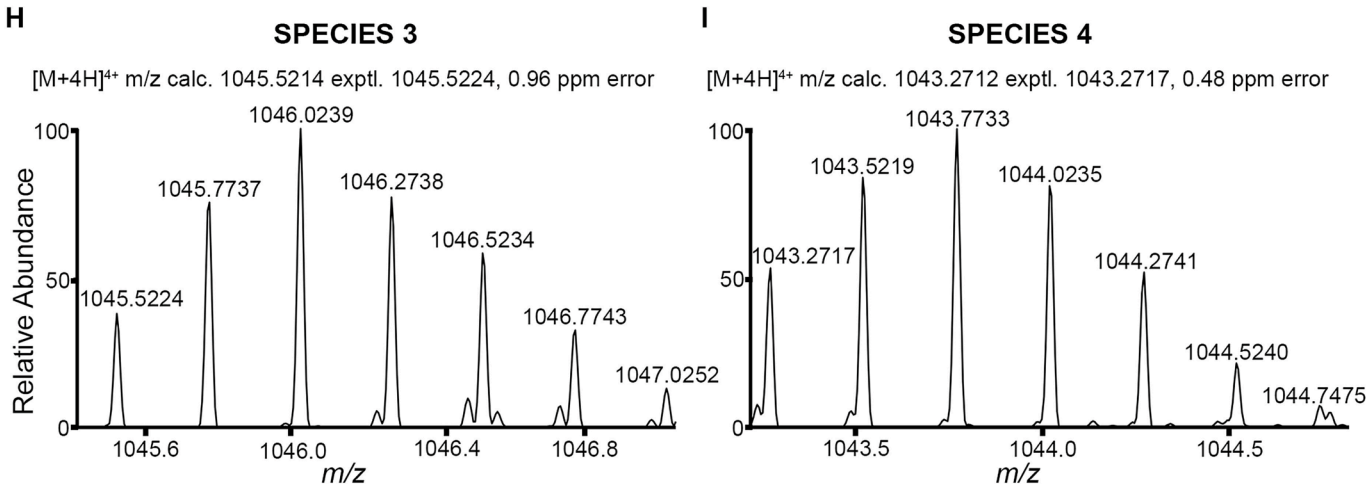

(caption on next page)

Fig. 2. Biochemical and mass spectrometry analysis of conformationally restricted variants of SiRFP shows domain crossover. (A) cysJ⁻ E. coli (Baba et al., 2006) transformed with SiRFP-WT, empty vector, SiRFP-X, or SiRFP-△ were grown on M9 or LB media. Both conformationally restricted variants are functionally active with slightly reduced ability to complement the cysJ⁻ deficiency. (B) SDS-PAGE analysis of SiRFP variants under reducing (+, containing β-mercaptoethanol (BME) in the loading dye) or non-reducing (-, without BME in the loading dye) shows higher order complexes form. Lanes 1, 3 and 5 are SiRFP-WT, SiRFP-X and SiRFP-△ samples with BME (+); lanes 2, 4 and 6 are SiRFP-WT, SiRFP-X and SiRFP-△ without BME (-). The main band at 67 kDa represents either free or crosslinked SiRFP subunits within the SiRFP octamer. Higher order bands (*) indicate the presence of polymerized subunits. (C) UV–visible spectra of SiRFP variants (left) or SiR variants (right) show the expected signals, indicating the variants are properly folded with cofactors bound. (D) Schematic showing the identified crosslinked peptides from MS. Species 1 from E121C/D556C (but otherwise WT within that peptide) identified a crosslink between E121C (pink; in the Fld domain) and N556C (blue; in the FNR domain). Species 2 and 3 from E121C/D556C/H132Q co-expressed with E121C/D556C/D545E, identified intramolecular crosslinking. H132Q (green) and D545E (orange) are uniquely identifiable markers present in his-SiRFP-X or CBP-SiRFP-X, respectively. Species 4 shows that intermolecular crosslinking is present between his-SiRFP-X and CBP-SiRFP-X. (E) A domain crossover, minimal SiRFP dimer derived from 6EFV (Tavolieri et al., 2019) allowed us to engineer the E121C (pink, from the subunit colored blue)/N556C (blue, from the subunit colored pink) disulfide as well as the H132Q (green) or D545E (orange) positions to uniquely identify the crosslinked peptides using MS. The edge-to-edge distance between the flavins in this crossover dimer is 4.4 Å, within the Moser-Dutton ruler for fast electron transfer (Moser et al., 1992). (F-I) MS identifies each of the species described in (D). Raw spectra for each can be found in Fig. S2.

Table 1
SANS parameters for SiRFP-X, SiRFP-△ and DSiR-X.[a]

Protein	% D_2O	Oligomeric state	Domain or protein composition	R_g (Å)[b]	D_{max} (Å)	MW (kDa)	SANS MW[c] (KDa)	Conc (mg/ml)
SiRFP-X	100	octamer (α_8)	X-linked SiRFP	78.5 ± 0.2	230	571	582.5	7
SiRFP-△	100	octamer (α_8)	SiRFP deletion in linker (△-AAPSQS)	78.6 ± 0.7	255	571	585.2	3
DSiR-X (DSiR-X0)	0	dodecamer ($\alpha_8\beta_4$)	SiRFP-X/ DSiRHP	98.3 ± 1.1	283	826	873	4
DSiR-X (DSiR-X41)	41	dodecamer ($\alpha_8\beta_4$)	SiRFP-X[d]/ DSiRHP	110 ± 7.2	324	826		10
DSiR-X (DSiR-X86)	86	dodecamer ($\alpha_8\beta_4$)	SiRFP-X/ DSiRHP[d]	78.5 ± 0.4	226	826		4
DSiR-X (DSiR-X100)	100	dodecamer ($\alpha_8\beta_4$)	SiRFP-X/ DSiRHP	82.9 ± 0.2	251	826		4
SiR-X	100	dodecamer ($\alpha_8\beta_4$)	SiRFP-X/ SiRHP	103.4 ± 0.6	310	802	873	2
SiR-△	100	dodecamer ($\alpha_8\beta_4$)	SiRFP-X/ SiRHP	99.9 ± 0.8	303	802	873	3

[a] Measurements were performed at three instrument configuration settings.
[b] R_g values are obtained from *P(r)* calculations.
[c] Data at full contrast were used to obtain SANS MW.
[d] The contrast-matched component.

linear relationship between R_g^2 and inverse contrast ($\triangle\bar{\rho}^{-1}$), suggesting a less asymmetric dodecamer when the SiRFP subunits are crosslinked (Fig. 4C). Nevertheless, the higher R_g^2 values remain at + α, suggesting that the center of mass (COM) of the component with higher scattering length density (DSiRHP) is at the periphery of the complex, whereas SiRFP-X's COM is central to the complex (Table 2).

3.4. SiRFP-WT behaves more like SiRFP-X than SiRFP-△

Chemical reduction of monomeric SiRFP-60 alters the position of the Fld domain relative to the FNR domain (Murray et al., 2021), as it does in CPR (Freeman et al., 2017). Thus, we asked whether there is a similar change in the octameric complex of SiRFP-WT, SiRFP-X (with a full-length linker), or SiRFP-△ (with a shortened linker). To answer this question, we anaerobically prepared each sample under a nitrogen environment, chemically reduced the samples with DT and measured the neutron scattering properties in sealed banjo cuvettes. Reduction of SiRFP's flavins with DT is equivalent to reduction with NADPH, as previous studies have shown spectroscopically (Freeman et al., 2017; Tavolieri et al., 2019). Reduction did not alter the scattering at low *q* values, but both the WT and the crosslinked variants showed expansion of the R_g and D_{max} from 81.9 ± 0.5 Å/256 Å to 84.9 ± 0.5 Å/276 Å for the WT and 78.6 ± 0.2 Å/227 Å to 81.5 ± 0.2 Å/253 Å for SiRFP-X (Table 3, Fig. 5A and B, S4G-J, S5A and B, and Table S2). In contrast, reduction of SiRFP-△ resulted in no change to the R_g and a decrease in its D_{max} from 255 to 250 Å (Table 3, Fig. 5C, S4K-L and S5C). Guinier analysis shows that all samples are monodisperse (Fig. S3G-L).

3.5. Hemoprotein binding affects SiRFP's mobility

We previously observed that SiRHP binding impacts the relative position of the Fld and FNR domains through an unexplained mechanism (Murray et al., 2021). Therefore, we asked if restricting the positions of the Fld/FNR domains in conformationally restricted variants impacted the positioning of SiRHP within the complex. SiR-X and SiR-△ are monodisperse (Fig. S3M and N); scatter with a similar R_g and D_{max} (Table 1, Fig. 6A and B, S4M, and N, and Table S2); and show similar flexibility (Fig. 6C). SiR-△ is more compact as compared to SiRFP-△ based on the high *q* values represented in the Kratky analysis (Figs. 3C and 6C), suggesting that SiRHP binding reduces the flexibility of SiRFP. Interestingly, SiR-X was relatively less compact than SiRFP-X, suggesting that either crosslinking SiRFP subunits within the dodecamer had already induced the compaction or that crosslinking amongst SiRFP subunits impacts the effect of SiRHP binding to its partner(s) (Figs. 3C and 6C).

3.6. Modelling of the octamer predicts that the SiRFP octamerization domain is a central hub for a highly flexible complex with peripheral SiRHP monomers

The way in which SiRFP forms an octamer remains enigmatic. AlphaFold (Jumper et al., 2021; Roney and Ovchinnikov, 2022) predicts that it is a helical bundle of about 31 amino acids out of 52, perhaps a dimer of two four-helix bundles (Fig. S6), but with ill-defined regions at both the N- and C- termini.

To understand how this helical bundle could hold so many proteins together, we modeled the scattering envelope of SiRFP-X. The model

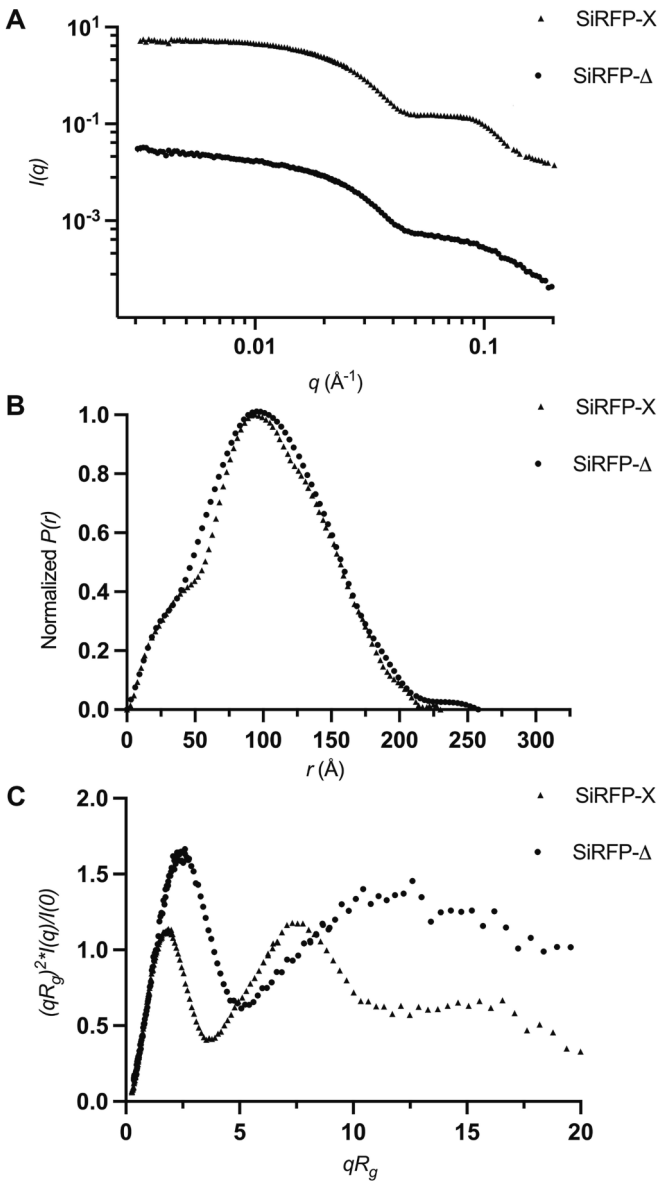

Fig. 3. Conformationally restricted SiRFP variants differ in their distance distribution and retain flexibility. (A) Scattering profiles of SiRFP-X and SiRFP-△. Data were rescaled for clarity and presented with error bars showing the standard deviation of *I(q)*. (B) *P(r)* plots of SiRFP-X and SiRFP-△. When compared to SiRFP-△ (D_{max} of 255 Å), SiRFP-X has a reduced D_{max} of 230 Å, indicating that SiRFP-X adopts a more compact conformation than SiRFP-△. (C) The dimensionless Kratky plots support the observation that SiRFP-X is more compact than SiRFP-△.

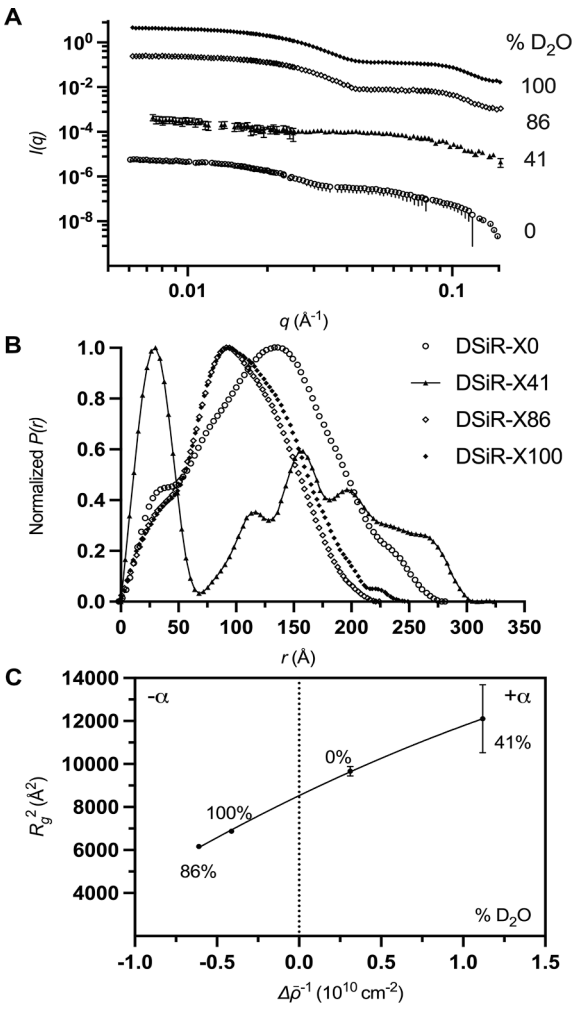

Fig. 4. NCV analysis on DSiR-X shows SiRHP remains peripheral and asymmetrically organized. (A) Scattering profiles of the DSiR-X contrast series at 0%, 41%, 86%, and 100% D_2O. (B) The *P(r)* plot of DSiR-X86 shows a reduced D_{max} upon binding to SiRHP but no change in the R_g stemming from restriction to its flexibility through the crosslinks. The *P(r)* of DSiR-X41 shows five peaks with a D_{max} of 324 Å. The first peak indicates the distance distribution from monomeric SiRHP whereas the peaks at higher r values correspond to the distances between each of the four SiRHP subunits. (C) Stuhrmann analysis shows that DSiR-X is less asymmetrically organized than DSiR (Murray et al., 2022), however, the positions of the SiRHP subunits remains peripheral to SiRFP, as in the WT complex. The plot was calculated using the scattering data in (A).

from DENSS (Grant, 2018) shows an eight-lobed structure with a central hub (Fig. 7A). Each lobe is about the size of a SiRFP monomer and the central hub is about the same dimensions as the predicted helical bundle. This is the first glimpse of how this highly dynamic, uniquely octameric, diflavin reductase assembles as the core of the SiR dodecamer.

To further understand the impact of the rigidified SiRFP core on the behavior of SiRHP, we used the contrast-matched DSiR-X86 and DSiR-X41, as well as SiR-X100, to model the envelope of each scattering feature. The envelope from DSiR-X86 scattering shows a continuous, eight-lobed structure with features similar to SiRFP-X but with reduced D_{max} values (Table 1, Fig. 7B, and Table S2). The envelope from DSiR-X41, however, shows four discrete globular densities with the distances between the furthest densities on the same scale as the largest

Table 2
Structural parameters for the components of DSiR-X.

Components		SiRFP-X	DSiRHP	DSiR-X
Contrast		2.40–5.65f_{D2O}[a]	4.85–5.58f_{D2O}[a]	
Experimental	R_g (Å)	78.5 ± 0.4	110 ± 7.2	98.3 ± 1.1
	D_{max} (Å)	226	324	283
Stuhrmann analysis	R_g (Å)	78.5 ± 0.2	115.3 ± 2.5	
	R_m (Å)			91.7 ± 0.3
	α			3780.8 ± 162
	β			111.6 ± 273.6
Parallel axis theorem	R_g (Å)	78.9 ± 0.2	115.1 ± 2.4	

[a] f_{D2O} is the D_2O fraction in the solvent.

Table 3
SANS parameter for oxidized and reduced SiRFP variants.[a]

Protein	R_g (Å)	D_{max} (Å)
SiRFP Oxidized	81.9 ± 0.5	256
SiRFP Reduced	84.9 ± 1.0	276
SiRFP-X Oxidized	78.6 ± 0.2	227
SiRFP-X Reduced	81.5 ± 0.2	253
SiRFP-△ Oxidized	78.5 ± 0.4	255
SiRFP-△ Reduced	78.6 ± 0.7	250

[a] Measurements were performed at two instrument configuration settings.

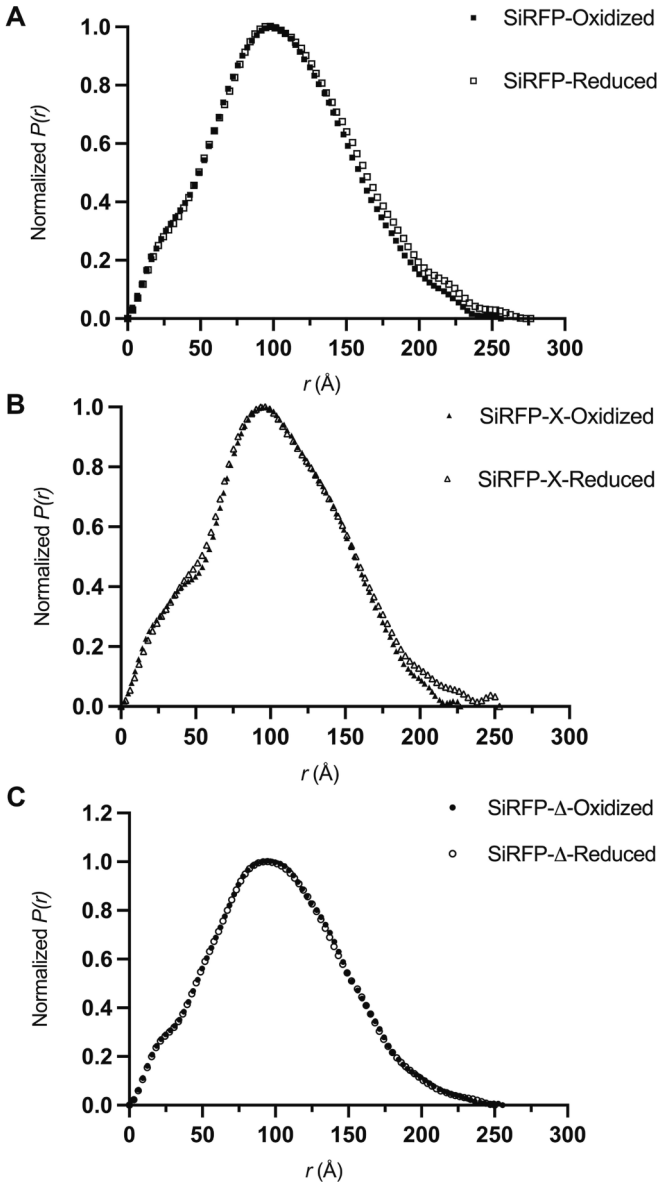

Fig. 5. Chemically reduced SiRFP variants show that SiRFP-WT behaves more like SiRFP-X than SiRFP-△. (A) *P(r)* plots of oxidized and chemically-reduced SiRFP. (B) *P(r)* plots of oxidized and chemically reduced SiRFP-X. (C) *P(r)* plots of oxidized and chemically reduced SiRFP-△. Reduced SiRFP-WT and SiRFP-X show an increase in D_{max} whereas SiRFP-△ shows a slight decrease in D_{max} compared to their oxidized variants.

dimension of the envelope derived from the full-scattering complex, SiR-X (Fig. 7C and D). Theoretical scattering curves calculated from each volume agree well with the experimental scattering (Fig. S7) (Franke et al., 2017; Grant, 2018). Theoretical scattering profiles calculated for the atomic-resolution models of SiRFP and SiRHP superimposed into the

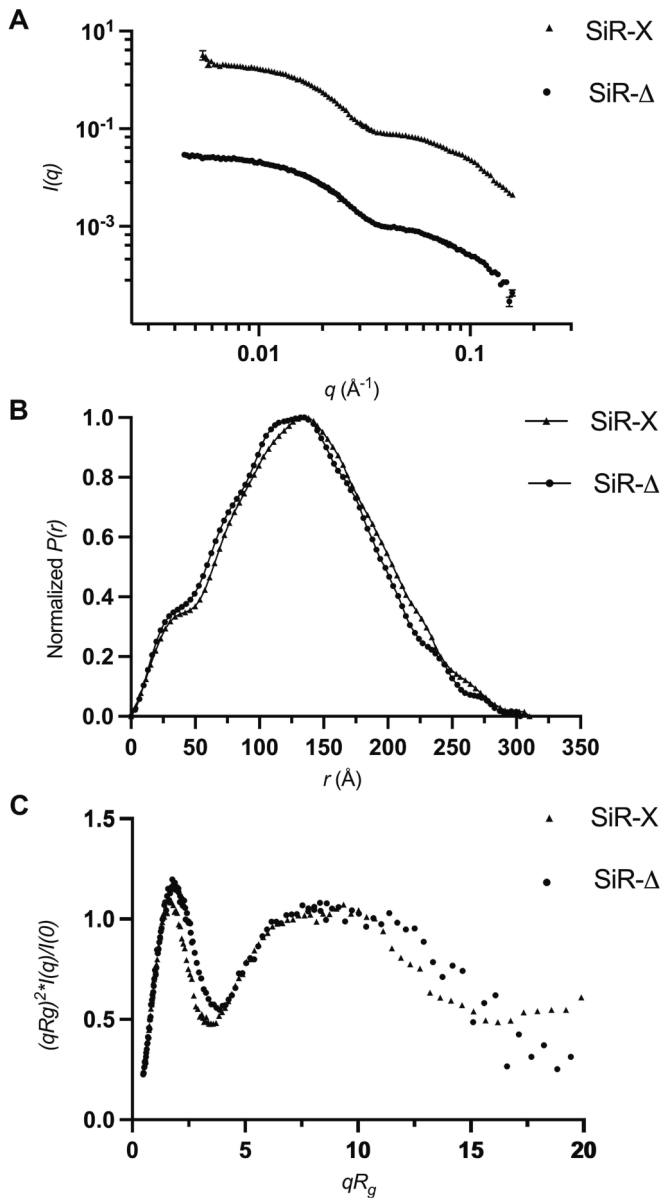

Fig. 6. SANS measurements on SiR-X and SiR-△ show that SiRHP binding affects SiRFP's mobility. (A) Scattering profiles of SiR-X and SiR-△. Data were rescaled for clarity and error bars represent the standard deviation of *I*(*q*). (B) The *P(r)* plots of SiR-X and SiR-△ show similar features overall. (C) The dimensionless Kratky plots show that SiRHP binding affects the mobility of SiRFP compared to free SiRFP (see Fig. 3C).

DENSS envelopes show the positioning of these structures to be reasonable, given the resolution limits of this approach (Fig. S8) (Grudinin et al., 2021; Schneidman-Duhovny et al., 2013).

4. Discussion

The conformational malleability of diflavin reductases has made structural studies of this family of oxidoreductases challenging, especially so when the reductase is present as an oligomer of flexibly tethered domains (Campbell et al., 2014; Gruez et al., 2000; Olteanu and Banerjee, 2001; Zhang et al., 2018). SiR's oligomerization is essential to its function and the relative structure of its components. Thus, comparing the impact of conformationally restricting the diflavin reductase in opposite ways – *i.e.* locking it closed (SiR-X) or open (SiR-

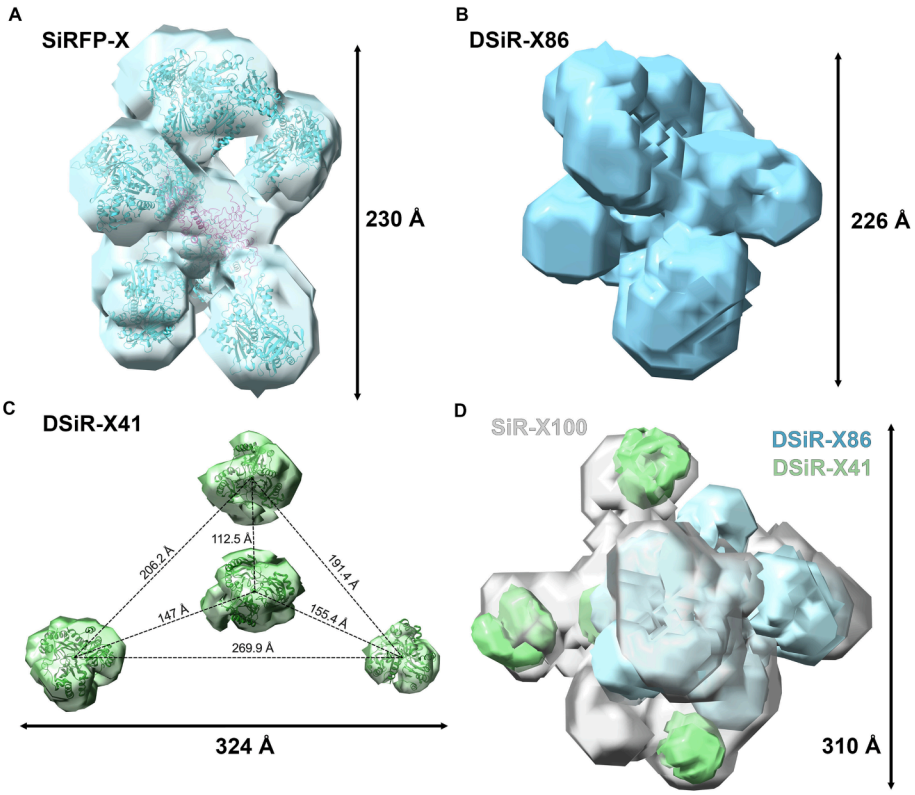

Fig. 7. Modelling of the octamer predicts that the SiRFP octamerization domain is a central hub for a highly flexible complex with peripheral SiRHP. (A) Eight copies of SiRFP modeled in AlphaFold (Jumper et al., 2021; Roney and Ovchinnikov, 2022) without their N-terminal 52 amino acids (blue ribbons) were docked into the SANS envelope of SiRFP-X (blue; generated in DENSS (Grant, 2018)). A model of the N-terminus was generated in AlphaFold (Jumper et al., 2021; Roney and Ovchinnikov, 2022), then assembled into an octameric helical bundle (pink) using HDOCK (Yan et al., 2020). This novel assembly fills the central void of the complex. The scale bar represents the D_{max} for each envelope. Figures were generated in ChimeraX (Pettersen et al., 2020). (B) The SANS envelope of DSiR-X86 (blue) shows a more compact shape (D_{max} of 226 Å) of SiRFP-X than as a free octamer (A). (C) The SANS envelope of DSiR-X41 from reconstituted DSiR-X shows four discrete globular subunits of SiRHP (green) docked with four monomeric SiRHP models (PDB 1AOP) (Crane et al., 1995). The distances between the COM for each subunit (dotted lines) were calculated in Chimera (Pettersen et al., 2004). (D) DSiR-X86 (blue) and DSiR-X41 (green) were superimposed on SiR-X100 (transparent grey), demonstrating a consistent organization.

△) – informs our understanding of this complex relationship.

Crosslinking experiments show that SiRFP undergoes domain crossover. That is, the FNR domain of one polypeptide can bind with the Fld domain of another and, perhaps, transfer electrons. Domain crossover has been observed in other diflavin reductases, but the large number of potential intermolecular interactions afforded by SiRFP's octameric structure makes it unique. The capacity for domain crossover in SiR presents numerous possible combinations for intramolecular Fld/FNR interactions within the same polypeptide of SiRFP or intermolecular Fld/FNR interactions within the adjoining polypeptides of SiRFP. Thus, there is a potential for variable dodecameric SiR complexes.

SiRHP binds at the periphery of SiR even while associated with SiRFP-X. SiRHP binding impacts the positioning of the Fld and FNR domains in monomeric SiRFP-60 (Murray et al., 2021), but the dodecameric SiR-X is functional even with the re-positioned domains that are restricted through the crosslink. However, the precise positioning of the SiRHP subunits around the octamer are impacted – interatomic distances between SiRHPs in SiR-WT are clustered in four discrete peaks (Murray et al., 2022) but in SiR-X there are five peaks, ranging from about 30–324 Å (Figs. 4B and 7C). This difference arises because there is an overlap between distances between two pairs of SiRHP-SiRHP subunits in SiR-WT (Murray et al., 2022) but the subunits are more evenly distributed in SiR-X, perhaps explaining why DSiRHP-X41 scatters with a slightly larger D_{max} than SiR-X. Nevertheless, this indicates that although the crosslinks in SiRFP do not interfere with SiRFP-X's ability to complement a SiRFP deficiency (Fig. 2A), they do impact the positioning of SiRHP.

Comparing oxidized to reduced SiRFP variants helps us understand the redox-dependent structural relationship between the Fld and FNR domain because the two variants with full-length linkers (WT and SiRFP-X) behave as expected, where reduction causes an overall expansion of the complex. In contrast, the variant with the truncated linker, SiRFP-△, does not change in its R_g and decreases slightly in its D_{max} (Table 3). Although a subtle observation, this informs our understanding of the structural arrangement of the octamer because it suggests that SiRFP-X is not crosslinked in a uniform fashion, so when both the crosslinks and the cofactors are reduced, it opens up as WT. If the linker is shortened, as in SiRFP-△, to limit intermolecular interactions, chemical reduction has no significant impact on the overall structure because there is no Fld domain to move away from its intermolecular FNR domain.

The structure of SiRFP's N-terminus is unknown because previously crystallized monomeric SiRFP lacks this octamerization domain and subsequent attempts at determining octameric SiRFP have been unsuccessful (Gruez et al., 2000; Tavolieri et al., 2019). AlphaFold (Jumper et al., 2021; Roney and Ovchinnikov, 2022) predicts that it contains a flexible N-terminus followed by a helix-turn-helix motif and then a largely unstructured region finally connecting it with the Fld domain. This explains why the octamer tolerates an N-terminal 6xHis fusion. More importantly, the unstructured region between the oligomerization domain and the first globular Fld domain provides additional degrees of freedom to allow the Fld and FNR domains to come together to transfer electrons between flavin cofactors and then open up to move them to the oxidase subunit while remaining tethered to seven other SiRFP subunits.

5. Conclusions

We show, for the first time, that SiRFP undergoes domain crossover such that the Fld domain of one polypeptide can interact with the FNR domain of a partner within its complex. This conformation could be functionally relevant because the enzyme retains its activity even when SiRFP is crosslinked in this mixed inter- and intramolecular conformation. Likewise, when the linker that allows such extreme flexibility is truncated, the enzyme retains activity. We also provide the first model of one possible arrangement of SiRFP subunits, including the predicted helical motif that forms the octameric SiRFP core. Predicted unstructured regions between the SiRFP octamerization domain and the first globular domain may underlie the ability for SiRFP to form the mixture of inter- and intramolecular interactions between SiRFP's Fld and FNR domains. SANS of reduced SiRFP variants measure the following: an opening of the complex that may enable intra- and intermolecular

interactions; the reversion of a compact SiRFP-X to that of a more open state upon changing cofactor redox state and crosslink reduction; and the hampered ability of SiRFP-△ to reposition its domains in such a fashion. Collectively, this study depicts SiR as a dynamic oxidoreductase complex capable of domain crossover, which we propose ensures its efficient functionality.

Data and code availability

All SANS data have been deposited in the SASBDB with the following codes: SASDS22 for SiRFP-X, SASDS32 for DSiR-X86, SASDS42 for DSiR-X41, SASDS52 for SiR-X, SASDS62 for SiRFP-△, SASDS72 for SiR-△, SASDS82 for DSiR-X0, SASDS92 for DSiR-X100, SASDSA2 for SiRFP-Reduced, SASDSB2 for SiRFP-X-Reduced, and SASDSC2 for SiRFP-△-Reduced.

Declaration of Competing Interest

The authors declare the following financial interests/personal relationships which may be considered as potential competing interests: M. Elizabeth Stroupe reports financial support was provided by National Science Foundation.

Data availability

Data will be made available on request.

Acknowledgments

We would like to thank Molecular Cloning Facility at Florida State University for helping us in constructing all required plasmids, Dr. Thomas D. Grant for helpful discussion regarding analysis of DENSS modelling and Dr. Christopher Stroupe and Dr. Raktin Roy for helpful discussions. A portion of this research used resources at Spallation Neutron Source, a DOE office of Science User Facility operated by the Oak Ridge National Laboratory. The Office of Biological and Environmental Research also supported work at the ORNL Center for Structural Molecular Biology. This work was supported by National Science Foundation grants MCB1856502 and CHE1904612 to M.E.S.

Appendix A. Supplementary data

Supplementary data to this article can be found online at https://doi.org/10.1016/j.jsb.2023.108028.

References

Askenasy, I., Pennington, J.M., Tao, Y., Marshall, A.G., Young, N.L., Shang, W., Stroupe, M.E., 2015. The N-terminal domain of Escherichia coli assimilatory NADPH-sulfite reductase hemoprotein is an oligomerization domain that mediates holoenzyme assembly. J. Biol. Chem. 290, 19319–19333.

Askenasy, I., Murray, D.T., Andrews, R.M., Uversky, V.N., He, H., Stroupe, M.E., 2018. Structure-function relationships in the oligomeric NADPH-dependent assimilatory sulfite reductase. Biochemistry 57, 3764–3772.

Baba, T., Ara, T., Hasegawa, M., Takai, Y., Okumura, Y., Baba, M., Datsenko, K.A., Tomita, M., Wanner, B.L., Mori, H., 2006. Construction of Escherichia coli K-12 in-frame, single-gene knockout mutants: the Keio collection. Mol. Syst. Biol. 2 (2006), 0008.

Campbell, M.G., Smith, B.C., Potter, C.S., Carragher, B., Marletta, M.A., 2014. Molecular architecture of mammalian nitric oxide synthases. Proc. Natl. Acad. Sci. U. S. A. 111, E3614-3623.

Crane, B.R., Siegel, L.M., Getzoff, E.D., 1995. Sulfite reductase structure at 1.6 A: evolution and catalysis for reduction of inorganic anions. Science 270, 59–67.

Dunne, O., Weidenhaupt, M., Callow, P., Martel, A., Moulin, M., Perkins, S.J., Haertlein, M., Forsyth, V.T., 2017. Matchout deuterium labelling of proteins for small-angle neutron scattering studies using prokaryotic and eukaryotic expression systems and high cell-density cultures. Eur. Biophys. J. 46, 425–432.

Durand, D., Vivès, C., Cannella, D., Pérez, J., Pebay-Peyroula, E., Vachette, P., Fieschi, F., 2010. NADPH oxidase activator p67(phox) behaves in solution as a multidomain protein with semi-flexible linkers. J. Struct. Biol. 169, 45–53.

Franke, D., Petoukhov, M.V., Konarev, P.V., Panjkovich, A., Tuukkanen, A., Mertens, H. D.T., Kikhney, A.G., Hajizadeh, N.R., Franklin, J.M., Jeffries, C.M., Svergun, D.I., 2017. ATSAS: a comprehensive data analysis suite for small-angle scattering from macromolecular solutions. J. Appl. Cryst. 50, 1212–1225.

Freeman, S.L., Martel, A., Raven, E.L., Roberts, G.C.K., 2017. Orchestrated domain movement in catalysis by cytochrome P450 reductase. Sci. Rep. 7, 9741.

Grant, T.D., 2018. Ab initio electron density determination directly from solution scattering data. Nat. Methods 15, 191–193.

Grudinin, S., Martel, A., Prevost, S. 2021. Pepsi-SAXS/SANS – small-angle scattering guided tools for integrative structural bioinformatics Acta Christ.

Gruez, A., Pignol, D., Zeghouf, M., Coves, J., Fontecave, M., Ferrer, J.L., Fontecilla-Camps, J.C., 2000. Four crystal structures of the 60 kDa flavoprotein monomer of the sulfite reductase indicate a disordered flavodoxin-like module. J. Mol. Biol. 299, 199–212.

Haque, M.M., Tejero, J., Bayachou, M., Kenney, C.T., Stuehr, D.J., 2018. A cross-domain charge interaction governs the activity of NO synthase. J. Biol. Chem. 293, 4545–4554.

Heller, W.T., Hetrick, J., Bilheux, J., Calvo, J.M.B., Chen, W.R., DeBeer-Schmitt, L., Do, C., Doucet, M., Fitzsimmons, M.R., Godoy, W.F., al., e., 2022. Drtsans: The Data Reduction Toolkit for Small-Angle Neutron Scattering at Oak Ridge National Laboratory. SoftwareX, 0-4.

Hopkins, J.B., Gillilan, R.E., Skou, S., 2017. improvements to a free open-source program for small-angle X-ray scattering data reduction and analysis. J. Appl. Cryst. 50, 1545–1553.

Ibel, K., Stuhrmann, H., 1975. Comparison of neutron and X-ray scattering of dilute myoglobin solutions. J. Mol. Biol. 93, 255–265.

Jumper, J., Evans, R., Pritzel, A., Green, T., Figurnov, M., Ronneberger, O., Tunyasuvunakool, K., Bates, R., Žídek, A., Potapenko, A., Bridgland, A., Meyer, C., Kohl, S.A.A., Ballard, A.J., Cowie, A., Romera-Paredes, B., Nikolov, S., Jain, R., Adler, J., Back, T., Petersen, S., Reiman, D., Clancy, E., Zielinski, M., Steinegger, M., Pacholska, M., Berghammer, T., Bodenstein, S., Silver, D., Vinyals, O., Senior, A.W., Kavukcuoglu, K., Kohli, P., Hassabis, D., 2021. Highly accurate protein structure prediction with AlphaFold. Nature 596, 583–589.

Lancaster, K.M., 2018. Revving up an artificial metalloenzyme. Science 361, 1071–1072.

Liu, F., Rijkers, D.T., Post, H., Heck, A.J., 2015. Proteome-wide profiling of protein assemblies by cross-linking mass spectrometry. Nat. Methods 12, 1179–1184.

Manalastas-Cantos, K., Konarev, P.V., Hajizadeh, N.R., Kikhney, A.G., Petoukhov, M.V., Molodenskiy, D.S., Panjkovich, A., Mertens, H.D.T., Gruzinov, A., Borges, C., Jeffries, C.M., Svergun, D.I., Franke, D., 2021. expanded functionality and new tools for small-angle scattering data analysis. J. Appl. Cryst. 54, 343–355.

Mirts, E.N., Petrik, I.D., Hosseinzadeh, P., Nilges, M.J., Lu, Y., 2018. A designed heme-[4Fe-4S] metalloenzyme catalyzes sulfite reduction like the native enzyme. Science 361, 1098–1101.

Mitani, F., 1979. Cytochrome P450 in adrenocortical mitochondria. Mol. Cell. Biochem. 24, 21–43.

Moore, P., 1981. On the estimation of the radius of gyration of the subunits of macromolecular aggregates of biological origin in situ. J. Appl. Chrysallogr. 14, 237–240.

Moore, P.B., Engelman, D.M., Schoenborn, B.P., 1974. Asymmetry in the 50S ribosomal subunit of Escherichia coli. PNAS 71, 172–176.

Moser, C.C., Keske, J.M., Warncke, K., Farid, R.S., Dutton, P.L., 1992. Nature of biological electron transfer. Nature 355, 796–802.

Murray, D.T., Weiss, K.L., Stanley, C.B., Nagy, G., Stroupe, M.E., 2021. Small-angle neutron scattering solution structures of NADPH-dependent sulfite reductase. J. Struct. Biol. 213, 107724.

Murray, D.T., Walia, N., Weiss, K.L., Stanley, C.B., Randolph, P.S., Nagy, G., Stroupe, M. E., 2022. Neutron scattering maps the higher-order assembly of NADPH-dependent assimilatory sulfite reductase. Biophys. J . 121, 1799–1812.

Olah, G.A., Rokop, S.E., Wang, C.L., Blechner, S.L., Trewhella, J., 1994. Troponin I encompasses an extended troponin C in the Ca(2+)-bound complex: a small-angle X-ray and neutron scattering study. Biochemistry 33, 8233–8239.

Olteanu, H., Banerjee, R., 2001. Human methionine synthase reductase, a soluble P-450 reductase-like dual flavoprotein, is sufficient for NADPH-dependent methionine synthase activation. J. Biol. Chem. 276, 35558–35563.

Pettersen, E.F., Goddard, T.D., Huang, C.C., Couch, G.S., Greenblatt, D.M., Meng, E.C., Ferrin, T.E., 2004. UCSF Chimera - A visualization system for exploratory research and analysis. J. Comput. Chem. 25, 1605–1612.

Pettersen, E.F., Goddard, T.D., Huang, C.C., Meng, E.C., Couch, G.S., Croll, T.I., Morris, J. H., Ferrin, T.E., 2020. UCSF ChimeraX: structure visualization for researchers, educators, and developers. Protein Sci.

Rambo, R.P., Tainer, J.A., 2011. Characterizing flexible and intrinsically unstructured biological macromolecules by SAS using the Porod-Debye law. Biopolymers 95, 559–571.

Roney, J.P., Ovchinnikov, S., 2022. State-of-the-art estimation of protein model accuracy using AlphaFold. Phys. Rev. Lett. 129, 238101.

Rousseau, F., Schymkowitz, J.W., Itzhaki, L.S., 2003. The unfolding story of three-dimensional domain swapping. Structure 11, 243–251.

Schaefer, W., Regula, J.T., Bähner, M., Schanzer, J., Croasdale, R., Dürr, H., Gassner, C., Georges, G., Kettenberger, H., Imhof-Jung, S., Schwaiger, M., Stubenrauch, K.G., Sustmann, C., Thomas, M., Scheuer, W., Klein, C., 2011. Immunoglobulin domain crossover as a generic approach for the production of bispecific IgG antibodies. PNAS 108, 11187–11192.

Schneidman-Duhovny, D., Hammel, M., Tainer, J.A., Sali, A., 2013. Accurate SAXS profile computation and its assessment by contrast variation experiments. Biophys. J . 105, 962–974.

Siddhanta, U., Presta, A., Fan, B., Wolan, D., Rousseau, D.L., Stuehr, D.J., 1998. Domain swapping in inducible nitric-oxide synthase. Electron transfer occurs between flavin and heme groups located on adjacent subunits in the dimer. J. Biol. Chem. 273, 18950–18958.

Siegel, L.M., Davis, P.S., 1974. Reduced nicotinamide adenine dinucleotide phosphate-sulfite reductase of enterobacteria. IV. The Escherichia coli hemoflavoprotein: subunit structure and dissociation into hemoprotein and flavoprotein components. J. Biol. Chem. 249, 1587–1598.

Smith, K.W., Stroupe, M.E., 2012. Mutational analysis of sulfite reductase hemoprotein reveals the mechanism for coordinated electron and proton transfer. Biochemistry 51, 9857–9868.

Tavolieri, A.M., Murray, D.T., Askenasy, I., Pennington, J.M., McGarry, L., Stanley, C.B., Stroupe, M.E., 2019. NADPH-dependent sulfite reductase flavoprotein adopts an extended conformation unique to this diflavin reductase. J. Struct. Biol.

Wang, M., Roberts, D.L., Paschke, R., Shea, T.M., Masters, B.S., Kim, J.J., 1997. Three-dimensional structure of NADPH-cytochrome P450 reductase: prototype for FMN- and FAD-containing enzymes. PNAS 94, 8411–8416.

Whitten, A., Cai, S., Trewhella, J., 2008. *MULCh*: modules for the analysis of small-angle neutron contrast variation data from biomolecular assemblies. J. Appl. Cryst. 41, 222–226.

Whitten, A.E., Jacques, D.A., Hammouda, B., Hanley, T., King, G.F., Guss, J.M., Trewhella, J., Langley, D.B., 2007. The structure of the KinA-Sda complex suggests an allosteric mechanism of histidine kinase inhibition. J. Mol. Biol. 368, 407–420.

Yan, Y., Tao, H., He, J., Huang, S.Y., 2020. The HDOCK server for integrated protein-protein docking. Nat. Protoc. 15, 1829–1852.

Zeghouf, M., Fontecave, M., Coves, J., 2000. A simplifed functional version of the Escherichia coli sulfite reductase. J. Biol. Chem. 275, 37651–37656.

Zhang, J., Martasek, P., Paschke, R., Shea, T., Siler Masters, B.S., Kim, J.J., 2001. Crystal structure of the FAD/NADPH-binding domain of rat neuronal nitric-oxide synthase. Comparisons with NADPH-cytochrome P450 oxidoreductase. J. Biol. Chem. 276, 37506–37513.

Zhang, H., Yokom, A.L., Cheng, S., Su, M., Hollenberg, P.F., Southworth, D.R., Osawa, Y., 2018. The full-length cytochrome P450 enzyme CYP102A1 dimerizes at its reductase domains and has flexible heme domains for efficient catalysis. J. Biol. Chem. 293, 7727–7736.